Quantitative phase velocimetry measures bulk intracellular transport of cell mass during the cell cycle

Soorya Pradeep[1], Thomas A. Zangle[1,2]*

[1] Department of Chemical Engineering, University of Utah, Salt Lake City, UT 84112, USA

[2] Huntsman Cancer Institute, University of Utah, Salt Lake City, UT 84112, USA

*Corresponding author. Email tzangle@chemeng.utah.edu

ABSTRACT

Transport of mass within cells helps maintain homeostasis and is disrupted by disease and stress. Here, we develop quantitative phase velocimetry (QPV) as a label-free approach to make the invisible flow of mass within cells visible and quantifiable. We benchmark our approach against alternative image registration methods, a theoretical error model, and synthetic data. Our method tracks not just individual labeled particles or molecules, but the entire flow of bulk material through the cell. This enables us to measure diffusivity within distinct cell compartments using a single approach, which we use here for direct comparison of nuclear and cytoplasmic diffusivity. As a label-free method, QPV can be used for long-term tracking to capture dynamics through the cell cycle.

INTRODUCTION

Orderly transport is essential for cell function and growth. To maintain homeostasis, cells continuously transport materials, including nutrients and bulk material into cells from the surrounding environment[1], ions through cell membranes[1], and liquids[2] and structural polymers into cell podia to drive cell motion[3]. In turn, cell transport can be impacted by disease[4] and stress[5, 6]. Measurement of transport within cells can therefore improve our understanding of cell behavior, disease, responses to environmental stresses and potential disease therapies. Fluorescent markers are the most commonly used tools to study transport within cells as they provide distinct signals with low background, making them easy to track[7, 8, 9, 10, 11]. Despite the wide use of fluorescent markers in transport studies, fluorescence come with the disadvantages of photobleaching and phototoxicity, which induce stress and modifies cell behavior[12, 13]. The number of components labeled at a time is also limited[14] and fluorescence tracking cannot measure velocities in untagged regions, limiting its ability to measure bulk material transport within cells.

Label-free methods offer an alternative to fluorescence for transport measurement. Label free methods, like phase contrast, differential interference contrast (DIC) and Raman imaging, have been applied to measure the dynamics of whole cells[15, 16], vesicles[17, 18], and lipid droplets[19] within cells. However, DIC measures phase gradients in just a single orientation, and phase-contrast images contain halos that make quantitative analysis difficult[20].

Quantitative phase imaging (QPI) is a label free imaging technique which measures the phase shift that occurs as light passes through a material with higher refractive index[21]. The phase shift measured with QPI is directly proportional to the distribution of dry mass in the sample[22]. QPI is, therefore, a better candidate for long-term transport studies within cells by providing quantitative data of the motion of bulk material within the cell. Previous work with QPI has used the contrast produced by localized variation in biomass density to track well-defined sub-cellular components as well as the overall average rate of mass motion[23, 24]. Spatial and temporal power spectra from QPI data have also been applied to quantify cell-average rheological properties[25, 26], dynamics of red blood cells[27], and localized diffusivities[28].

In this work we combine automated image velocimetry and label-free QPI to develop an approach we call quantitative phase velocimetry (QPV) that measures unsteady intracellular velocity fields capturing the bulk transport of cellular material over long times. To understand the sources of error

in QPV, we developed a theoretical model of QPV error that matches experimental results. We then apply QPV to measure dry mass transport inside cells during cell cycle progression. With this data, we quantify intracellular diffusion dynamics in the nucleus and cytoplasm over the cell cycle. We see nuclear diffusion decreases with cell cycle progression and cytoplasm diffusion reduces with G1 to S phase transition.

RESULTS

1. Development of QPV from QPI data

We developed QPV to measure intracellular dry mass velocity from QPI data (**figure 1**). QPI of retinal pigment epithelial (RPE) cells (**figure 1b**) shows the changing distribution of cell dry mass over time. In particular, QPI data show large regions of high mass density in nucleus, low mass podia, and small-scale puncta within cells that can serve as features for velocimetry (**figure 1b**). Taking the difference between QPI images over time illustrates the movement of mass captured by QPI (**figure 1c**). In this example, this difference image indicates an overall movement of the cell dry mass from the top right corner to the bottom left corner of the image frame. QPV uses these data to measure the movement of mass using the principles of particle image velocimetry (PIV). As expected in this individual, example cell, the distribution of intracellular dry mass velocity determined by QPV shows dry mass velocity vectors pointing from the top right to the left bottom of the frame, as well as localized deviation from that overall trend (**figure 1d**).

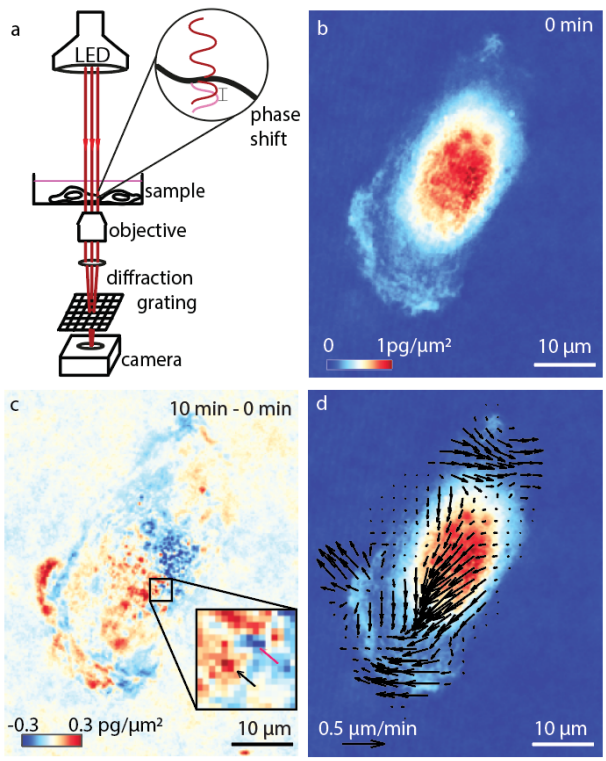

Figure 1. Quantitative phase velocimetry (QPV) measures intracellular dry mass movement. (a) Quantitative phase imaging (QPI) measures the phase shift of light passing through a cell, which is used to compute the dry mass distribution in cells over time. (b) Dry mass distribution in RPE cell imaged at 120X magnification, at $t = 0$ min. The scalebar indicates

10 µm length. (c) The difference in QPI mass distribution of the RPE cell in (b) from an image taken at t = 10 min later minus the image at 0 min reveals cell motion. The color scale shows the net displaced mass over this interval (red increase, blue decrease). The inset in (c) shows a 15x15 pixel interrogation window that illustrates the change in position of an individual subcellular feature from the position marked with a red arrow to the position marked with a black arrow. Colorbar shows dry mass difference between frame at time 0 and 10 minutes (red: large increase in mass, blue: large decrease in mass). (d) The resulting intracellular biomass velocity field computed using quantitative phase velocimetry (QPV). Velocity magnitude indicated with a 0.5 µm/min scalebar.

To choose the most compatible image registration method for developing QPV we compared the performance of methods commonly used for PIV: normalized cross-correlation (NCC)[29], optical flow reconstruction (OFR)[30], mutual information (MI)[31], and sum of squared differences (SSD)[32]. With each method, we estimated the resolution and accuracy of velocity measurement on fixed RPE and MCF7 cells moving at known velocity as a velocity standard, as fixed cells have the same distribution of intracellular features as living cells (**figure 2** and **figure S2-S3**). The displacement distribution computed by QPV of example fixed cells after a total of 1.5 µm downward stage motion shows uniform displacement distribution in all interrogation windows pointing in the direction of stage motion (**figure 2a** and **figure S2**).

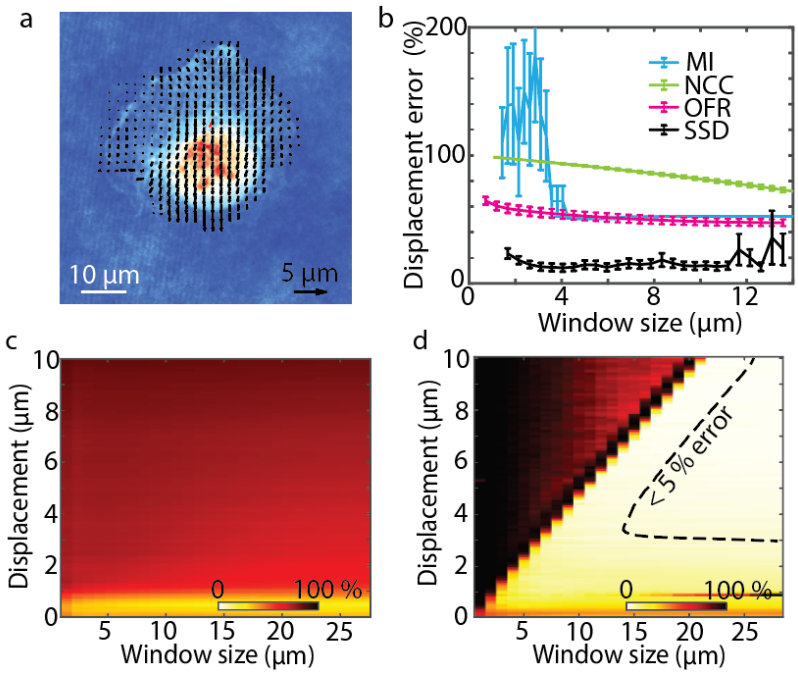

Figure 2. SSD image registration measures intracellular velocity from QPI data with higher accuracy than OFR, MI and NCC. (a) QPV on RPE fixed cell measures the intracellular displacement during microscope stage translation. (b) Comparison of mutual information (MI), normalized cross correlation (NCC), optical flow reconstruction (OFR) and

sum of squared difference (SSD) for intracellular velocity computation on QPI data at different interrogation window sizes shows SSD has highest accuracy at small window sizes (n = 11, error bar shows standard error of the mean, SEM). (c) Velocity accuracy versus both interrogation window size and displacements of RPE fixed cell using OFR shows that OFR is limited to measuring a very narrow range of displacements with acceptable accuracy (n = 11). Yellow/white – high accuracy, red/black – low accuracy. (d) QPV velocity measurement accuracy versus interrogation window size and displacements of fixed RPE cells show typically less than 10% error when the interrogation window size is smaller than the displacement to be measured with a region of less than 5% error indicated as a dashed line (n = 11).

We need the smallest possible interrogation window size for our velocimetry approach to get the highest spatial resolution of velocity field. We computed the measurement accuracy of 0.1 µm (0.42 x a single pixel) displacements of fixed cells using each method with interrogation window sizes ranging from 5 to 59 pixels (1.19 µm to 14 µm) square. This displacement error is the key determinant of the error in computed velocity as the time between frames is tightly controlled during imaging. Of the four methods tested, SSD and OFR performed better at smaller window sizes than MI and NCC which work moderately well with large windows (**figure 2b** and **figure S3a)**.

The image registration method used for QPV should also perform well over a wide range of displacements as cells typically display a wide range of motion from sub-pixel movement in the nucleus to highly deforming multiple pixel displacements in the podia regions of the cytoplasm. Based on their performance at small window sizes, we further measured displacement error with SSD and OFR for displacements from 0.1 to 10 µm and interrogation window sizes from 1 to 14 µm. The results for OFR with fixed RPE and MCF7 cells shows greater than 50% error for displacement measurements above 1 µm at all interrogation window sizes tested (**figure 2c** and **figure S3c**). Performance of OFR at large displacements can be improved using Gaussian blurring[33] (**figure S4**). However, Gaussian blurring comes at the cost of losing the ability to resolve small-scale differences in deformation within cells. On the other hand, SSD gives an error of less than 10% for any displacement, as long as the window size for the calculation is at least as large as the displacement itself and less than 5% for a subset of this region (**figure 2d**). We also evaluated SSD has less error than OFR in displacement direction measurement (**figure S5**). SSD also performs better than OFR for different cells (**figure S6**). Therefore, considering accuracy, spatial resolution and the ability to measure a wide range of displacements, we chose SSD as the image registration method for QPV.

2. Theoretical modelling of displacement measurement accuracy

To understand the sources of errors in QPV, we developed a model that account for key parameters that contribute to measurement noise. These are: the size range of cell features which impacts Brownian diffusion of cell components and the ability to visualize displacement with the interrogation window size chosen, the interrogation window size which determines the maximum measurable displacement, and the optical resolution limit of the microscope.

To study how the distribution of spatial features and noise influence the performance of QPV, we generated synthetic data consisting of uniform circles (**figure 3a** top middle) and non-uniform-sized circles (**figure 3a** top right) with sizes matched to the average particle sizes observed in RPE and MCF7 cells (**figure 3b** and **figure S7b)**. Perlin noise was added to synthetic data to match the continuous local variation background noise in our QPI data (**figure 3a** bottom middle and bottom right). Perlin noise thus has similar power spectrum as the background noise in QPI, and reduces the magnitude of the power spectral density (**figure S7b**). The power spectra of the RPE fixed cell, MCF7 fixed cell, and polystyrene beads imaged at 20X magnification match best with the power spectrum of non-uniform synthetic data with Perlin noise (**figure 3b** and **figure S7b**). Therefore, based on this power spectrum analysis, QPI images are best approximated as having as non-uniform spatial features with added low spatial frequency noise.

Converting frequency to equivalent particle size shows that the features potentially able to be tracked by QPV range in size from organelle-size puncta of mass to the entire cell (**figure 3c-d**). To account for the range of feature sizes captured by QPI and their individual contributions to measurement error, we compute the theoretical error for all particle sizes in a cell up to 40 µm, the size of a whole cell (**figure 3e**, **figure S9c-d**), then perform a weighted average of these particle errors based on the power spectrum for the cell (**figure 3c**, **figure S9b**). The resulting prediction of the error in displacement magnitude (**figure 3f**, **figure S9e**) are in good agreement with the experimentally computed error for both RPE (**figure 3g)** and MCF7 cells (**figure S9f**). Both predicted and measured error show large error if the displacement is larger than the window size as well as large error when the displacement is less than the diffraction limit (0.48 µm in our case). We also observe reasonable agreement in the predicted and measured displacement direction error (**figure S10**). Application of this model and validation allows us to predict the minimum window size for accurate intracellular velocimetry. For example, for RPE and MCF7 cells imaged at 120X

magnification every 1 minute, the typical observed range of displacement varies from 0 to 5 pixels outside of the very fast moving podia. Therefore, we use a 15 by 15 pixel interrogation window, which corresponds to an area of 12.75 μm^2.

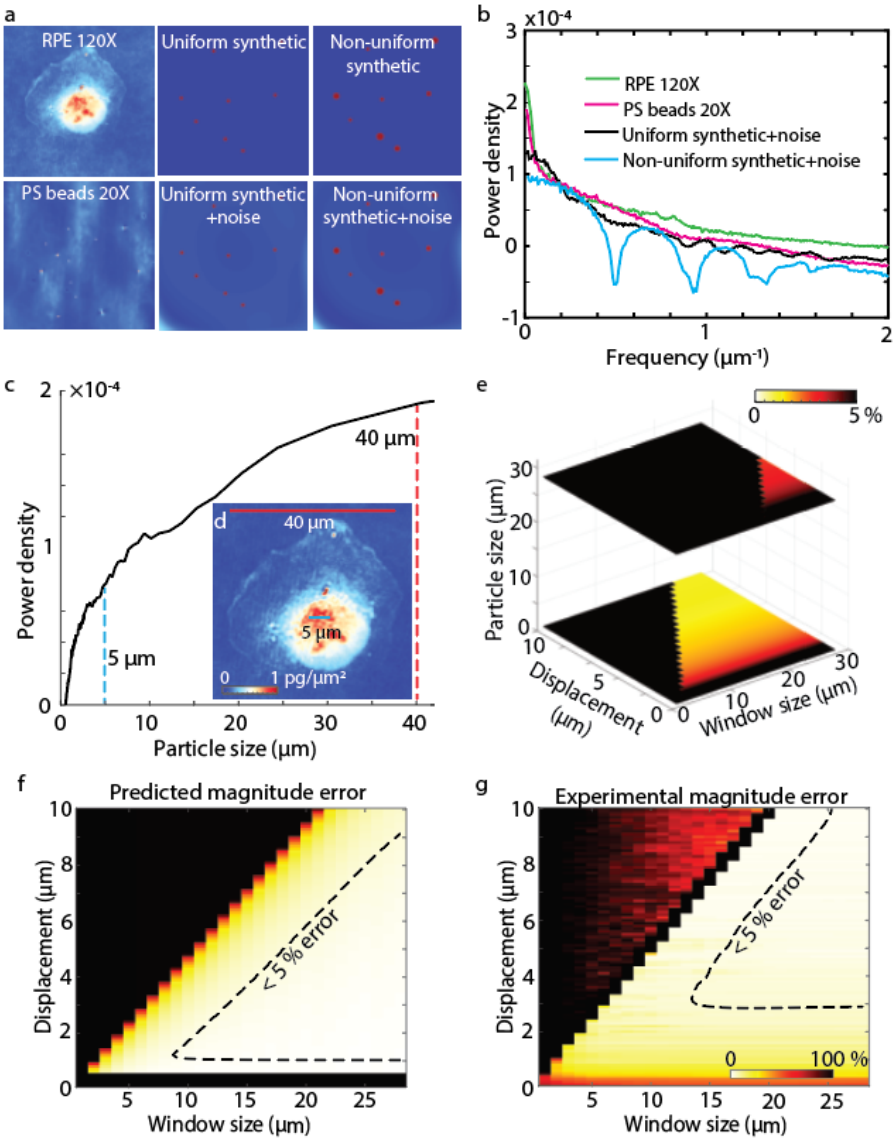

Figure 3. Modelled QPV displacement measurement error agrees with experimental measurements. (a) Comparison of background corrected QPI image of RPE fixed cell at 120 X (top left) and polystyrene beads at 20X (bottom left) to synthetically generated uniform and non-uniform circle data, with added Perlin noise (top middle and right) and without added Perlin noise (bottom middle and right) (b) Power spectrum of the QPI data (green and magenta) and synthetic data with noise (black) in (a) shows the similarity of QPI data to the non-uniform circle synthetic data. (c) 2 μm organelle structure inside 40 μm RPE fixed cell illustrating the range of features captured by QPI. Scale bars show 5 μm (blue) and 40 μm (red). Colormap shows dry mass density in pg/μm^2. (d) Power spectral density versus effective particle size of RPE fixed

cells (n = 3). Power spectral density corresponding to both 5 µm and 40 µm structures is indicated. (e) Theoretical displacement estimation error at 2 and 30 µm particle size for all tested displacements and window sizes. (f) Averaging the size dependent model results as in (e), weighted by the actual distribution of particle sizes (c) gives a predicted error which is in agreement with the (g) measured error from the matched RPE cell using experimental data. Colormaps in (f) and (g) are the same.

3. Application of QPV for measurement of intracellular displacements

QPV tracks both overall cellular deformation as well as the motion of individual regions within cells. As a method based on QPI, which measures dry mass distributions[22], QPV measures displacement of dry mass. Sample results for an RPE cell are shown in **figure 4**. The deformation of a uniform grid overlayed on the RPE cell image from time 0 minutes (**figure 4a**) to 30 minutes (**figure 4b**) shows compression of the grid points in the nuclear region and the spacing out of points in the podia region (**figure 4b**), reflecting the observed compression of the cell as its podia move upward within the image frame (**movie S1**). Each square enclosed by four grid points in **figure 4a** represents a volume encompassing a specific quantity of dry mass in the cell. Using QPV, we track each region of dry mass as it moves and deform with time. The motion of five such volumes in the nuclear and cytoplasmic regions of the indicated RPE cell shows upward movement of the control volumes and the movement of the cell over 30 minutes (**figure 4c-d** and **movie S2**). From these tracks, we can see that mass originating from the central region of the cell are more direction oriented with smaller scale fluctuations than mass originating in the lower density regions of the cytoplasm.

QPV data quantifies the overall velocity of bulk mass transport of each region within the cell. The mean velocity distribution over 30 minutes in the cell shows a higher average velocity in the cytoplasm region, with a moderate velocity in the nuclear region (**figure S11a**). To more systematically assess differences between the cytoplasm and nucleus, we segmented the nuclear region from the cytoplasm of the RPE cell using the fluorescent images of an expressed FUCCI marker[34]. Separating the velocities in the nucleus and cytoplasm and comparing them to the cell centroid velocity showed no difference as the cell nucleus and bulk of the cytoplasm moves with the cell (n = 59 cells, **figure S11b**). We compute the deformation velocity as the velocity of the volumes inside the nucleus and cytoplasm relative to the cell centroid velocity. The deformation velocity map overlayed on the RPE cell (**figure 4e**), shows a similar distribution as the overall distribution of intracellular velocities **(figure S11a**). However, the velocity magnitude in the

regions showing the smallest deformations, such as the nucleus, are reduced to around zero (**figure 4e**). The average deformation velocity from the nucleus and cytoplasm of the cell also reflects a larger deformation in the cytoplasm compared to the cell nucleus (**figure 4f**). Thus, the nuclei of RPE cells move more in line with the overall cell body relative to the cytoplasm, with the podia in particular exhibiting a larger velocity relative to that of the whole cell. We also observe higher activity in the cell nucleus and cytoplasm in S phase (**figure 4f**) perhaps due to the combined action of DNA replication supplemented by histone transcription and synthesis[35].

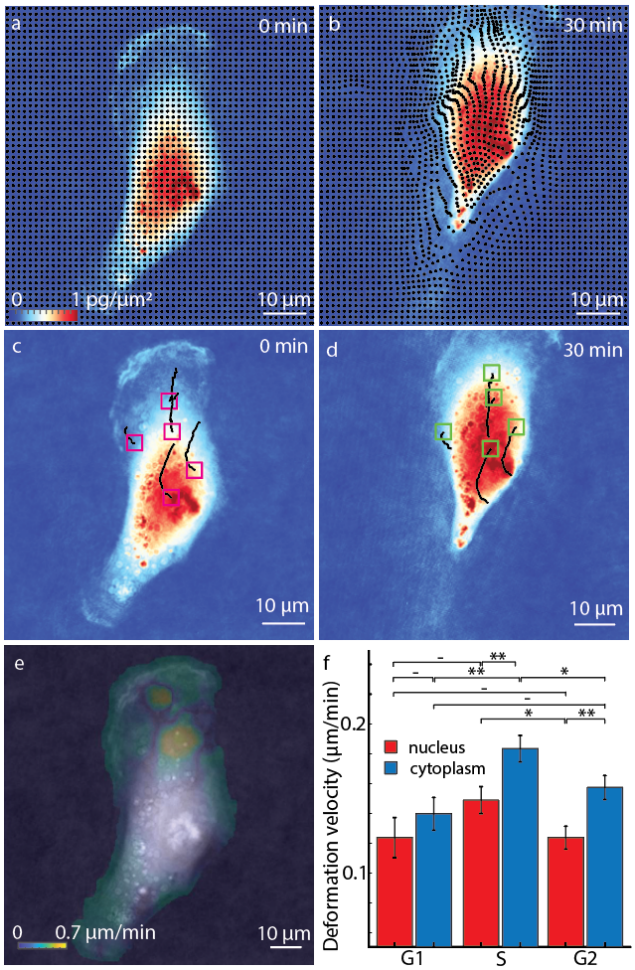

Figure 4. QPV shows spatial and temporal dynamics of biomass motion within cells. (a) Grid markers depict 4 by 4 pixel intracellular volume centroids overlayed on an RPE cell at 120 X magnification (b) which deforms from (a) to (b) due to movement of the cells in 30 minutes. (c) Dry mass inside control volumes initial positions marked using magenta boxes travel along the black line to reach the final positions indicated using green boxes in (d) in 30 minutes. (e) Deformation velocity, the whole cell velocity subtracted intracellular velocity distribution of dry mass, inside the RPE cell (f) Deformation velocity of dry mass in nucleus and cytoplasm of RPE cells, shows higher deformation in cytoplasm than nucleus (n = 59, error bars show standard error of the mean). * $p < 0.05$, ** $p < 0.01$.

4. Decreasing intracellular diffusion with cell cycle progression

Using QPV, we tracked the intracellular dynamics of mass within every control volume within the cell (**Figure 4c-d**) to measure transport of mass continuously for eight hours while simultaneously monitoring cell cycle progression with the FUCCI cell cycle indicator[34]. From these data, we then performed the mean squared displacement (MSD) analysis of the deformation, or displacement relative to cell centroid displacement, of all tracked intracellular mass from QPV of RPE cells in cell cycle (**figure 5**). The slope and intercept of the MSD plot was used to measure the anomalous constant and diffusion coefficient, respectively, of each intracellular region tracked with QPV (**figure 5a-c**). To validate our MSD calculation, we compare the anomalous and diffusion constants of live RPE cells to fixed cells moved artificially on a stage that show effectively zero diffusivity (**figure S12**). Nuclear boundaries were determined by alignment to fluorescence images of FUCCI cell cycle markers (**figure S13**). These data indicate that although cytoplasmic material exhibits a larger range of displacements than material within the nucleus (**figure 5d-e**), these displacements indicate a lower average effective diffusivity (**figure S14a**). Both nuclear and cytoplasmic diffusion were consistent with moderately sub-diffusive, anomalous diffusion (**figure S14b**).

The average diffusion coefficient was slightly higher in the nucleus than in the cytoplasm with wide variation (**figure S14a**). To understand this variation, we binned the diffusion coefficient based on cell cycle phase (**figure 5f**, **figure S15a**). These data indicate that the nuclear diffusion coefficient reduces with cell cycle progression and cytoplasm diffusion coefficient reduces through G1 to S phase transition and agree with estimates of spatially variable intracellular diffusivity over similar time scales using quantum dots[36]. As a method that tracks mass of intracellular components, we can apply QPI to determine the dependence of the measured diffusivity of each control volume on its mass. We find a moderate fit to a power law ($R = 0.2$) with a scaling exponent of -0.233 (**figure 5h**). This is close to the expected scaling of $D \sim m^{-1/3}$ that would be predicted from Stokes-Einstein, assuming mass scales with the cube of effective particle size, but with significant deviation at the level of individual control volumes. We estimated the effective size of particles tracked by QPV from the power spectra of QPI images (**figure 3a**), limited to particles that are within the window size used for QPV. This yields a roughly constant effective particle size through the cell cycle (**figure S15b**).

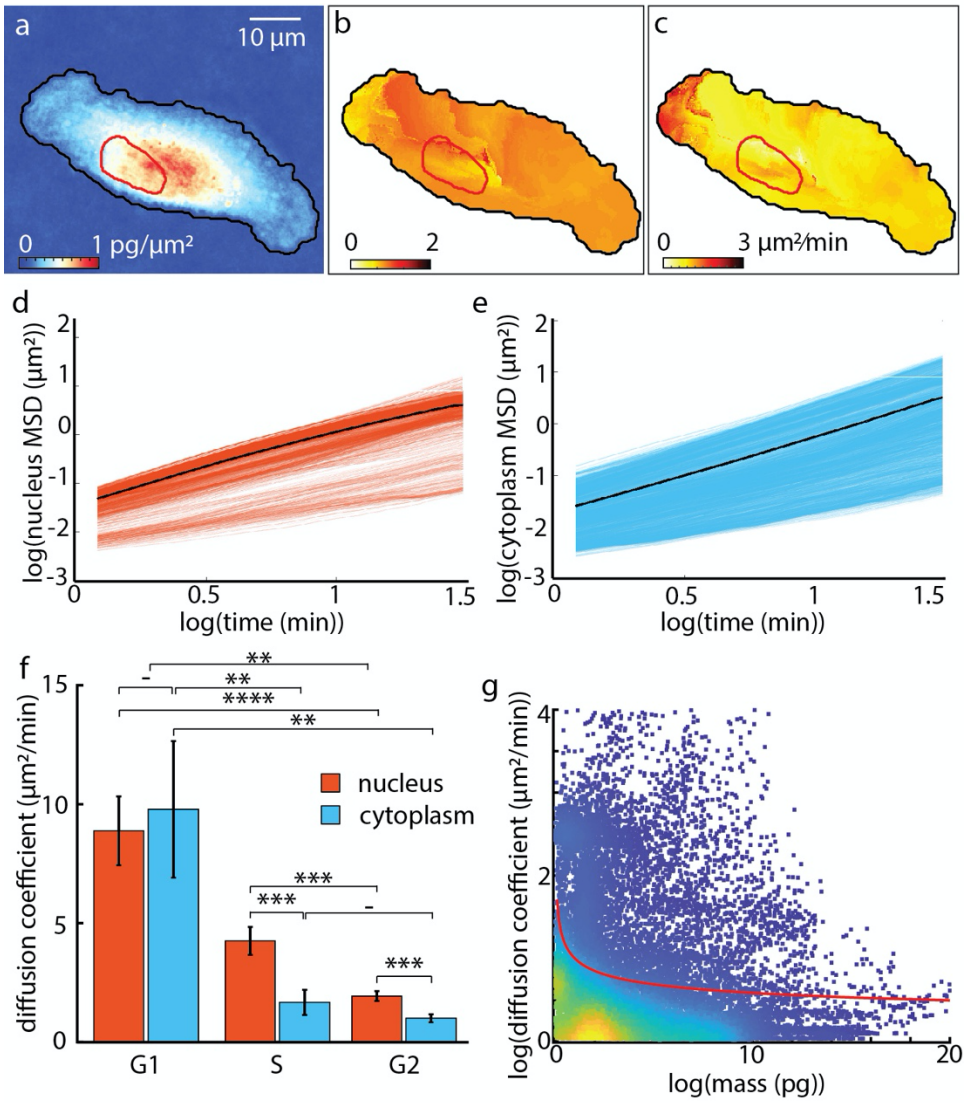

Figure 5. Mean squared displacement (MSD) analysis shows reduced diffusion coefficient in RPE cells with cell cycle progression. (a) QPI image of individual RPE cell with red nuclear and black cytoplasmic boundary shown. (b) Anomalous constant distribution within the RPE cell from (a). (c) Diffusion coefficient distribution within the RPE cell from (a). (d) Logarithm of MSD vs time lag of intracellular volumes in the nucleus of the RPE cell in (a). The black line shows the mean of all nuclear volumes. Black line shows the mean of all cytoplasmic volumes. (f) Nuclear and cytoplasmic diffusion coefficients in RPE cells over the cell cycle from $n = 119$ cells. Error bars show standard error of the mean. (g) Diffusion coefficient versus mass for all regions tracked inside RPE cells. Red line shows best fit power law which has a scaling exponent of -0.233.. ** $p < 0.01$, *** $p < 1\text{x}10^{-3}$, **** $p < 1\text{x}10^{-4}$.

DISCUSSION

We developed QPV to measure unsteady velocity fields of bulk intracellular transport from QPI. In contrast to bulk transport across the cell membrane and into cells, the bulk intracellular transport measured with QPV is the transport of all cellular material within the cell. As a label-free method, QPV can directly be applied to measure mass transport within cells over long periods, such as throughout the cell cycle, and to make direct comparisons between cellular compartments. We also applied QPV to quantify the transport properties of subcellular trajectories to measure intracellular effective diffusivity through the cell cycle.

Our model of error contributions to QPV points towards possible improvements. One key insight is that the particle size distribution is critical in determining the accuracy of QPV. This suggests that a high-pass filtering scheme may improve accuracy of QPV by reducing the effective particle size. However, this would come at the loss of applicability to tracking whole cell displacements, as the resulting velocity fields would be for a subset of intracellular particles. We also note that, though Brownian motion was found to be a key limit to the accuracy of velocity estimation for previous applications of PIV to microscopy data to measure flow within microchannels[37, 38], we found the influence of Brownian motion to have a small impact on QPV. We estimate an impact of <3% for the smallest particle sizes imaged and negligible impact for the largest particles tracked.

QPV has a number of advantages over alternative approaches for studying mass transport within cells. Unlike many other label-free methods, QPV automatically tracks intracellular features based on PIV. Additionally, as a label-free method, QPV avoids issues with phototoxicity, photobleaching, or label dilution over time, while still giving results for intracellular diffusivity that are comparable in magnitude to methods requiring labels. Another major advantage of QPV is that it uses the same analysis for both nucleus and cytoplasm, allowing direct comparisons between these two compartments that are difficult to label consistently with other approaches. Overall, this work suggests that QPV is a valuable tool to study intracellular transport and biophysics.

REFERENCES

1. Palm W, Thompson CB. Nutrient acquisition strategies of mammalian cells. *Nature* 2017, **546**(7657)**:** 234-242.

2. Keren K, Yam PT, Kinkhabwala A, Mogilner A, Theriot JA. Intracellular fluid flow in rapidly moving cells. *Nat Cell Biol* 2009, **11**(10)**:** 1219-1224.

3. Ridley AJ, Schwartz MA, Burridge K, Firtel RA, Ginsberg MH, Borisy G*, et al.* Cell Migration: Integrating Signals from Front to Back. *Science* 2003, **302**(5651)**:** 1704.

4. Kuwahara M, Marumo F. [Diseases caused by disorders of membrane transport: an overview]. *Nihon rinsho Japanese journal of clinical medicine* 1996, **54**(3)**:** 581-585.

5. Kodiha M, Stochaj U. Nuclear transport: a switch for the oxidative stress-signaling circuit? *J Signal Transduct* 2012, **2012:** 208650.

6. Sviderskaya EV, Jazrawi E, Baldwin SA, Widnell CC, Pasternak CA. Cellular Stress Causes Accumulation of the Glucose Transporter at the Surface of Cells Independently of their Insulin Sensitivity. *The Journal of Membrane Biology* 1996, **149**(2)**:** 133-140.

7. Progatzky F, Dallman MJ, Lo Celso C. From seeing to believing: labelling strategies for in vivo cell-tracking experiments. *Interface Focus* 2013, **3**(3)**:** 20130001.

8. Sheetz MP, Spudich JA. Movement of myosin-coated fluorescent beads on actin cables in vitro. *Nature* 1983, **303**(5912)**:** 31-35.

9. Sankaran J, Wohland T. Fluorescence strategies for mapping cell membrane dynamics and structures. *APL Bioeng* 2020, **4**(2)**:** 020901.

10. Liebel M, Ortega Arroyo J, Beltrán VS, Osmond J, Jo A, Lee H*, et al.* 3D tracking of extracellular vesicles by holographic fluorescence imaging. *Science Advances* 2020, **6**(45)**:** eabc2508.

11. Shaban HA, Barth R, Recoules L, Bystricky K. Hi-D: nanoscale mapping of nuclear dynamics in single living cells. *Genome Biol* 2020, **21**(1)**:** 95.

12. Jensen EC. Types of Imaging, Part 2: An Overview of Fluorescence Microscopy. *The Anatomical Record* 2012, **295**(10)**:** 1621-1627.

13. Dixit R, Cyr R. Cell damage and reactive oxygen species production induced by fluorescence microscopy: effect on mitosis and guidelines for non-invasive fluorescence microscopy. *Plant J* 2003, **36**(2)**:** 280-290.

14. Valm AM, Oldenbourg R, Borisy GG. Multiplexed Spectral Imaging of 120 Different Fluorescent Labels. *PLoS One* 2016, **11**(7)**:** e0158495.

15. House D, Walker ML, Zheng W, Wong JY, Betke M. Tracking of cell populations to understand their spatio-temporal behavior in response to physical stimuli. 2009 IEEE Computer Society Conference on Computer Vision and Pattern Recognition Workshops; 2009 20-25 June 2009; 2009. p. 186-193.

16. Li K, Miller ED, Chen M, Kanade T, Weiss LE, Campbell PG. Cell population tracking and lineage construction with spatiotemporal context. *Med Image Anal* 2008, **12**(5)**:** 546-566.

17. Chaphalkar AR, Jawale YK, Khatri D, Athale CA. Quantifying Intracellular Particle Flows by DIC Object Tracking. *Biophys J* 2021.

18. Zhang W, Xu Y, Chen G, Wang K, Shan W, Chen Y. Dynamic single-vesicle tracking of cell-bound membrane vesicles on resting, activated, and cytoskeleton-disrupted cells. *Biochim Biophys Acta Biomembr* 2019, **1861**(1)**:** 26-33.

19. Nan X, Potma EO, Xie XS. Nonperturbative chemical imaging of organelle transport in living cells with coherent anti-stokes Raman scattering microscopy. *Biophys J* 2006, **91**(2)**:** 728-735.

20. Vicar T, Balvan J, Jaros J, Jug F, Kolar R, Masarik M*, et al.* Cell segmentation methods for label-free contrast microscopy: review and comprehensive comparison. *BMC Bioinformatics* 2019, **20**(1)**:** 360.

21. Barer R. Interference microscopy and mass determination. *Nature* 1952, **169**(4296)**:** 366-367.

22. Zangle TA, Teitell MA. Live-cell mass profiling: an emerging approach in quantitative biophysics. *Nat Methods* 2014, **11**(12)**:** 1221-1228.

23. Wang Z, Millet L, Mir M, Ding H, Unarunotai S, Rogers J*, et al.* Spatial light interference microscopy (SLIM). *Opt Express* 2011, **19**(2)**:** 1016-1026.

24. Sandoz PA, Tremblay C, van der Goot FG, Frechin M. Image-based analysis of living mammalian cells using label-free 3D refractive index maps reveals new organelle dynamics and dry mass flux. *PLoS Biol* 2019, **17**(12)**:** e3000553.

25. Eldridge WJ, Steelman ZA, Loomis B, Wax A. Optical Phase Measurements of Disorder Strength Link Microstructure to Cell Stiffness. *Biophys J* 2017, **112**(4)**:** 692-702.

26. Nguyen TL, Polanco ER, Patananan AN, Zangle TA, Teitell MA. Cell viscoelasticity is linked to fluctuations in cell biomass distributions. *Sci Rep* 2020, **10**(1)**:** 7403.

27. Park Y, Diez-Silva M, Popescu G, Lykotrafitis G, Choi W, Feld MS*, et al.* Refractive index maps and membrane dynamics of human red blood cells parasitized by Plasmodium falciparum. *Proceedings of the National Academy of Sciences* 2008, **105**(37)**:** 13730-13735.

28. Ma L, Rajshekhar G, Wang R, Bhaduri B, Sridharan S, Mir M*, et al.* Phase correlation imaging of unlabeled cell dynamics. *Sci Rep* 2016, **6:** 32702.

29. Sarvaiya JN, Patnaik S, Bombaywala S. Image Registration by Template Matching Using Normalized Cross-Correlation. 2009 International Conference on Advances in Computing, Control, and Telecommunication Technologies; 2009 28-29 Dec. 2009; 2009. p. 819-822.

30. Vig DK, Hamby AE, Wolgemuth CW. On the Quantification of Cellular Velocity Fields. *Biophys J* 2016, **110**(7)**:** 1469-1475.

31. Pluim JPW, Maintz JBA, Viergever MA. Mutual-information-based registration of medical images: a survey. *IEEE Transactions on Medical Imaging* 2003, **22**(8)**:** 986-1004.

32. Hisham MB, Yaakob SN, Raof RAA, Nazren ABA, Wafi NM. Template Matching using Sum of Squared Difference and Normalized Cross Correlation. 2015 IEEE Student Conference on Research and Development (SCOReD); 2015 13-14 Dec. 2015; 2015. p. 100-104.

33. Sharmin N, Brad R. Optimal Filter Estimation for Lucas-Kanade Optical Flow. *Sensors* 2012, **12**(9)**:** 12694-12709.

34. Zielke N, Edgar BA. FUCCI sensors: powerful new tools for analysis of cell proliferation. *Wiley Interdiscip Rev Dev Biol* 2015, **4**(5)**:** 469-487.

35. Ma Y, Kanakousaki K, Buttitta L. How the cell cycle impacts chromatin architecture and influences cell fate. *Front Genet* 2015, **6:** 19.

36. Li H, Dou SX, Liu YR, Li W, Xie P, Wang WC*, et al.* Mapping intracellular diffusion distribution using single quantum dot tracking: compartmentalized diffusion defined by endoplasmic reticulum. *J Am Chem Soc* 2015, **137**(1)**:** 436-444.

37. Santiago JG, Wereley ST, Meinhart CD, Beebe DJ, Adrian RJ. A particle image velocimetry system for microfluidics. *Exp Fluids* 1998, **25**(4)**:** 316-319.

38. Meinhart CD, Wereley ST, Santiago JG. A PIV algorithm for estimating time-averaged velocity fields. *J Fluid Eng-T Asme* 2000, **122**(2)**:** 285-289.

39. Bon P, Maucort G, Wattellier B, Monneret S. Quadriwave lateral shearing interferometry for quantitative phase microscopy of living cells. *Opt Express* 2009, **17**(15)**:** 13080-13094.

40. Edelstein A, Amodaj N, Hoover K, Vale R, Stuurman N. Computer Control of Microscopes Using µManager. *Current Protocols in Molecular Biology* 2010, **92**(1)**:** 14.20.11-14.20.17.

41. Barer R, Joseph S. Refractometry of Living Cells. *Quarterly Journal of Microscopical Science* 1954, **s3-95**(32)**:** 399.

42. Lucas BD, Kanade T. An iterative image registration technique with an application to stereo vision. *Proceedings of the 7th international joint conference on Artificial intelligence - Volume 2*. Vancouver, BC, Canada: Morgan Kaufmann Publishers Inc.; 1981. pp. 674–679.

43. xb H. a function with the simplest form to calculate the mutual information (https://www.mathworks.com/matlabcentral/fileexchange/42165-a-function-with-the-simplest-form-to-calculate-the-mutual-information). *MATLAB Central File Exchange. Retrieved March 11, 2019*.

44. Bon P, Maucort G, Wattellier B, Monneret S. Quadriwave lateral shearing interferometry for quantitative phase microscopy of living cells. *Opt Express* 2009, **17**(15)**:** 13080-13094.

METHODS

Microscopy

We performed QPI with an Olympus IX83 inverted microscope (Olympus Corporation, Japan) in brightfield with a 100X, 1.3 numerical aperture oil-immersion objective, and 1.2X magnifier to match the Nyquist criteria with a quadri-wave lateral shearing interferometry wavefront sensing camera [39] (Phasics SID4-4MP (Phasics, France) camera). 120 ms exposure with red LED illumination (623 nm, DC2200, Thorlabs, USA) was used for QPI image acquisition. We used MATLAB (Mathworks, USA) for automated image acquisition. We connected the illumination sources, Retiga camera and stage with MicroManager open-source microscopy software [40]. The Olympus IX83 microscope (Olympus corporation, Japan) and Phasics camera were connected directly through MATLAB. QPI images were captured every 1 minute and fluorescence images every 30 minutes at 30 imaging positions in every dataset. A flipping mirror arrangement (IX3-RSPCA, Olympus Corporation. USA) enabled alternate fluorescent and QPI. X-Cite 120LED light source (Excelitas technologies, USA) and Retiga R1 camera (Cairn research Ltd, UK) at 300 ms exposure were used for the fluorescence, with an Olympus U-FBNA filter cube for green mAG fluorophore and Semrock mCherry-B-000 filter cube (IDEX health & science, USA) for imaging the red mKO2 fluorophore. Uniform 37°C and 5% CO_2 conditions were maintained using an Okolab stage-top incubator (Okolab, Italy) and custom-built objective heating collar, temperature controlled by Thorlabs temperature controller (Thorlabs, USA). For live cell imaging, cells were plated in Ibidi μ-high treated dishes at 30% confluence. Four sets of 30 live cells were imaged every for 8 hours for every imaging session.

Cell culture

Cell culture procedures complied with the University of Utah BSL-2 guidelines. MCF7 (mammary epithelium) cell lines donated by Welm lab (HCI, Utah) were cultured in Dulbecco's modified eagle's medium (DMEM) (Gibco™ 11330057, Thermo Fisher Scientific, USA) with 10% fetal bovine serum (FBS) (Corning™ 35015CV, Fisher Scientific, USA). mKO2-hCdt1 and mAG-hGem tagged FUCCI expressing RPE-1 cells from Edgar lab (HCI, Utah), prepared by Yiqin Ma, were cultured in Gibco DMEM with 10% FBS and 5% Penicillin-Streptomycin. Penicillin-Streptomycin was removed while imaging the cells. Cells were split 1 to 6 to 1 to 3 ratio at confluence less than 80% at a frequency based on their growth rate.

Cell FUCCI tagging

RPE cells donated by the lab of Bruce Edgar (University of Utah) were received FUCCI tagged with mAG-hGem and mKO2-hCDt1. Cells express the mKO2 tag on Cdt1 in the nucleus during G1 phase (red nucleus), added mAG tag on Geminin in the nucleus during S phase (yellow nucleus due to combination of red mKO2 and green mAG) and the loss of mKO2 with the onset of G2 phase (green nucleus). The fluorescent image of the FUCCI tagged nuclei captured every 30 minutes was segmented using the k-mean algorithm (available as a built-in function in MATLAB) and overlapped with the QPI image.

Mycoplasma testing

We DAPI (Fisher-NC9677247) stained fixed cells, grown 80 to 90 % confluent, after permeabilizing the nuclei using methanol at 4ºC, to test for mycoplasma contamination. The DAPI stained cells were imaged using a Retiga R1 camera at 500 ms exposure time and Olympus U-FUNA filter cube, illuminated by X-Cite 120LED. We checked the presence of DAPI stained puncta outside the nucleus as an indicator for mycoplasma contamination.

Initial processing of QPI data

The Phasics SID4BIO camera for QPI uses a modified Hartmann mask diffraction grating to compute the phase gradient in two orthogonal directions which were converted to phase measurements using the Phasics Matlab SDK (Phasics, France). Phase shift was converted to dry mass using an assumed specific refractive increment of 0.18 μm^3/pg for cell material [22]. The phase shift of light (ϕ) expressed as an optical path length is directly related to the dry mass (m) at a given pixel through the specific refractive increment (α) [41] as:

$$m = \frac{1}{\alpha} \int \phi dA \tag{1}$$

where A is the area of each pixel of the phase shift image. QPI images were then background corrected by fourth order polynomial curve fitting to regions in the phase image outside of cells.

Fixed cell imaging

RPE and MCF7 cells were plated in Ibidi μ-high treated dish at 40% confluence. Cells were fixed by removing cell culture media, washing with PBS and incubating in 4% paraformaldehyde (PFA)

at 37ºC for 10 minutes. The PFA was further removed, cells washed with PBS, refilled with fresh PBS and sealed and stored until imaging. During imaging, the dish was heated to 37ºC on Okolab stage-top incubator 20 minutes prior to imaging to avoid condensation. Cells were imaged at each 0.05 µm step stage translation in the vertical direction.

Image registration

Sum of squared differences (SSD)

SSD was then performed on overlapping discretized interrogation windows of 15 by 15 pixels, spaced by 1 pixel, in the background corrected QPI image. The SSD of two image regions was computed as:

$$SSD(i,j) = \sum_{i=0}^{M}\sum_{j=0}^{N}\left(f(i,j) - g(i+u, j+v)\right)^2 \tag{2}$$

where *f* and *g* are the two interrogation windows from successive images to be matched using SSD with *i* and *j* the location of pixels comprising the image, *M* and *N* are the width and length of the image in pixels and *u* and *v* are the displacement introduced at each iteration of the SSD calculation.

Normalized cross correlation (NCC)

NCC between interrogation windows was measured using the MATLAB function *normxcorr2*. The displacement of the highest pixel in the correlation plane from the center pixel was used to compute the displacement of the each interrogation window.

Optical flow reconstruction (OFR)

OFR developed by Lucas and Kanade [42] measures the transport of intensity profile in images, given by

$$\frac{\Delta I}{\Delta t} = \frac{I(t+\Delta t) - I(t)}{\Delta t} = -v.\nabla I \tag{3}$$

Here $I(t+\Delta t)$ and $I(t)$ are intensity of images time Δt apart, in our case 1 minute. We used the code available from [30] for OFR displacement calculation. The *BlurSize* parameter for blurring image using Gaussian blurring before OFR in code was set to 1. The *BlurStd* parameter was set to 1,2,5,8 and 12 for understanding impact of Gaussian blurring (figure S4 c and d).

Mutual Information (MI)

MI was computed using a method implemented in MATLAB that extracts mutual information from the joint histogram and joint entropy of the registered images that was adapted to perform mutual information (MI) image registration calculation on sliding interrogation windows inside grayscale QPI images [43].

Quantitative phase velocimetry

Our implementation of QPV is based on the SSD image registration method [32] applied to 15 by 15 pixel (3.57 by 3.57 μm) interrogation windows within cells. A magnified view of one 15 by 15 pixels interrogation window inside an example cell difference image (**figure 1c**) shows the movement of individual cell components (pointed by red arrow) to a position on the left side of the window, pointed by black arrow (15 by 15 pixel inset in **figure 1c)**. SSD produces the lowest sum of squared difference when such patterns of mass within an interrogation window overlap between two displaced windows from successive imaging frames (**figure S1a)**. Gaussian fitting on the 3 by 3 pixel region neighborhood around the lowest value of the computed SSD gives sub-pixel localization of displacements (**figure S1b)**. This results in the measured displacements that form the basis of QPV (**figure S1c**). Spurious velocities were removed using a conditional median filter, thus retaining the original values of subcellular velocity computed. From the known time gap between frames set during cell imaging, we compute the velocity of mass transport from these displacement measurements (**figure 1d**). Processing was performed using computational resources allocated by the Center for High Performance Computing (CHPC) at the University of Utah. Code is available on GitHub (https://github.com/ZangleLab).

Calculation of measurement error

The error of displacement magnitude (E_{mag}) was calculated as:

$$E_{mag} = \frac{(D_{real} - D_{measured})}{D_{real}} \times 100\ \% \tag{4}$$

where D_{real} is the actual magnitude of displacement introduced by movement of stage, and $D_{measured}$ is the average measured displacement magnitude.

Direction error (E_{dir}) was computed as the angle between the computed and actual displacement vector:

$$E_{dir} = \theta_{real} - \theta_{measured} \tag{5}$$

θ_{real} is the actual angle of displacement introduced by stage and $\theta_{measured}$ is the average angle measured by image registration method.

QPV error model

Power spectra of the cell images was azimuthally averaged to convert power density image to 2-dimensional plot of power density vs frequency.

We estimated the optical diffraction limit as:

$$Diffraction\ limit = \frac{\lambda}{NA} \tag{6}$$

where λ is the wavelength of light and NA is the numerical aperture of the objective used for imaging, assuming that the illumination NA = 0 to generate a spatially coherent plane wave for QPI [44]. The code for constructing the particle size dependent error model is also available on GitHub (https://github.com/ZangleLab).

Deformation velocity

The whole cell velocity was computed based on tracking segmented cell centroids. The cell nucleus was segmented from cytoplasm using k-means segmentation algorithm on FUCCI fluorescence images. Cytoplasm and nucleus mask were used to separate subcellular 3-minute displacement tracks in corresponding regions and used to compute cytoplasm and nuclear velocities separately. The average cell centroid velocity was subtracted from all intracellular velocities and averaged in cytoplasm and nucleus to compute the deformation velocity of cytoplasm and nucleus.

MSD analysis

Relation between MSD and time lag (τ) is given by

$$<MSD> = 4D\tau^{\alpha} \tag{7}$$

D is the diffusion coefficient and α is the anomalous constant. The proportionality constant is 4D as the tracking is two-dimensional. The effective particle size (d_p) is obtained from power spectrum of QPI image of the cell, weighting the particle size by the power spectrum density, within the limit of particle sizes visible by the interrogation window size.

Statistics

Welch's two-tailed t test with unequal variances was used to calculate the significance of differences between experimental groups. Error bars are reported as the standard error of the mean based on the number of cells in each test group.

ACKNOWLEDGMENTS

This work was supported by the University of Utah and NIH K25CA157940. We thank Dr. Bruce Edgar's lab, Dr. Yiqin Ma at the Huntsman Cancer Institute, University of Utah for donation of FUCCI tagged RPE cells. We also thank Dr. Alana Welm's lab at Huntsman Cancer Institute, University of Utah for donation of MCF7 cells. Finally, the support and resources from the Center for High Performance Computing at the University of Utah are gratefully acknowledged.

AUTHOR CONTRIBUTIONS

Conceptualization: TZ; Experiments: SP; Theoretical formulation: SP, TZ; Funding acquisition: TZ; Investigation: SP, TZ; Code: SP, TZ; Supervision: TZ

ADDITIONAL INFORMATION

The authors declare that they have no competing interests.